



Dual strategies for enhancing piezoelectric catalytic ability of energy storage BiOBr@Bi₄O₅Br₂ heterojunction: Interfacial electric field and intrinsic polarization electric field



Bixin Zhang ^a, Guoqiang Tan ^{a,d,*}, Ao Xia ^{a,**}, Zeqiong Wang ^a, Xiongtao Wu ^a, Linxin Guo ^a, Chunyan Zeng ^a, Ying Liu ^a, Tian Liu ^a, Qian Yang ^a, Lixiong Yin ^{a,**}, Wenlong Liu ^{b,**}, Huijun Ren ^c, Sizhe Fan ^a

^a Shaanxi Key Laboratory of Green Preparation and Functionalization for Inorganic Materials, School of Material Science and Engineering, Shaanxi University of Science & Technology, Xi'an 710021, China

^b School of Electronic Information and Artificial Intelligence, Shaanxi University of Science & Technology, Xi'an 710021, China

^c School of Culture and Education, Shaanxi University of Science & Technology, Xi'an 710021, China

^d Shaanxi Stomatological Medical Equipment and Equipment Engineering Technology Research Center, Xianyang 712000, China

ARTICLE INFO

Keywords:

Interface electric field
Intrinsically polarized electric field
Storage piezoelectric catalysis
Around the clock

ABSTRACT

An energy storage BiOBr@Bi₄O₅Br₂ heterojunction piezoelectric catalyst was prepared by homogeneous nucleation hydrothermal crystallization. The interfacial electric field enhances the polarization electric field and the piezoelectric effect of the heterojunction, the stored electron and hole concentrations are 94.23 and 86.17 $\mu\text{mol}\cdot\text{g}^{-1}$, respectively, and d_{33} is increased to 6.29 $\text{nm}\cdot\text{V}^{-1}$. In the dark for 50 min, the degradation rates of tetracycline, ciprofloxacin and bisphenol A caused by energy storage and positive piezoelectric effect are 63.44%, 75.95% and 73.90%, respectively, and it has good dark cycle stability and dark repair. Under the visible and near infrared light, the double localized surface plasmon resonance effects of heterojunction electron-hole storage and the enhanced series polarized electric field accelerate the migration rate of stored electrons and holes. This work provides a new idea of the preparation of around the clock energy storage piezoelectric catalytic materials from traditional energy storage bismuth-based nanomaterials with the intrinsic polarization electric field.

1. Introduction

Antibiotics such as tetracycline (TC) and ciprofloxacin (CIP) have been discharged into the body because they cannot be completely absorbed by organisms, and have entered rivers, lakes and groundwater through water circulation, which has destroyed the water balance, increased the drug resistance of bacteria and endangered human health [1]. As a potential environmental and ecological hazard, it is urgent to eliminate antibiotics in water [2,3]. In the BiOBr crystal, the alternating arrangements of [Bi₂O₂]²⁺ layer and [Br₂]²⁻ layer positive and negative charge layers generate a polarized electric field, which can improve the bulk charge separation efficiency and is used as a photocatalytic material for eliminating antibiotics in water [4,5]. However, due to the

over-positive position of the conduction band (CB), and the intensity of the intrinsic polarization electric field is small, and electrons and holes are easy to recombine, resulting in the low bulk charge separation efficiency and the low catalytic activity of antibiotics [6]. It is necessary to enhance the intrinsic polarization electric field intensity of BiOBr to improve its bulk charge separation efficiency and its catalytic degradation ability to eliminate antibiotics in water [7]. Compared with BiOBr, the charge density around the [Bi-O] layer in Bi_xO_yBr_z is higher than that around the [Br-Br] layer, and the uneven charge distribution between the [Bi-O] and [Br-Br] layers will enhance the intensity of the polarized electric field, thus improving its bulk charge separation efficiency [8]. Therefore, researchers have prepared a series of Bi_xO_yBr_z photocatalysts: Bi₃O₄Br [9], Bi₄O₅Br₂ [10], Bi₅O₇Br [11], Bi₁₂O₁₇Br₂

* Corresponding author at: Shaanxi Key Laboratory of Green Preparation and Functionalization for Inorganic Materials, School of Material Science and Engineering, Shaanxi University of Science & Technology, Xi'an 710021, China.

** Corresponding authors.

E-mail addresses: tan3114@163.com (G. Tan), xiaao@sust.edu.cn (A. Xia), ylx@sust.edu.cn (L. Yin), lwl1020@126.com (W. Liu).

[12] and $\text{Bi}_{24}\text{O}_{31}\text{Br}_{10}$ [13,14]. The $\text{Bi}_x\text{O}_y\text{Br}_z$ polarization electric field is enhanced by bismuth-rich strategy, and the catalytic degradation ability is improved [15].

However, the separation efficiency of electrons and holes by a single $\text{Bi}_x\text{O}_y\text{Br}_z$ is still limited, so the separation of electrons and holes can be promoted by constructing a $\text{BiOBr}/\text{Bi}_x\text{O}_y\text{Br}_z$ heterojunction with energy band matching, and the photocatalytic activity of the heterojunction can be improved [16–18]. However, the $\text{BiOBr}/\text{Bi}_x\text{O}_y\text{Br}_z$ heterojunction prepared by the research is to improve the redox ability of Type II heterojunctions and Z-scheme heterojunctions by regulating the interface electric field between BiOBr and $\text{Bi}_x\text{O}_y\text{Br}_z$. The LSPR effect of electrons and holes stored in the polarized electric field of BiOBr and $\text{Bi}_x\text{O}_y\text{Br}_z$ crystals have not been studied in the whole spectral range to eliminate the catalytic degradation ability of antibiotics in water.

The double LSPR effect of free electrons and holes stored in heterojunction can make its light absorption cover the whole solar spectrum, which is often used to improve the light absorption ability of photocatalyst [19,20]. Zhang et al. [21] obtained Ti_3C_2 MXene by HF etching and ultrasonic crushing of Ti_3AlC_2 , which distributed holes on its surface and bounded electrons in the crystal. Under NIR light irradiation, the dual LSPR effect of Ti_3C_2 MXene excited surface holes into high-energy hot holes, directly oxidizing antibiotics and organic pollutants. Electrons bound in the crystal lagged behind the excitation of high-energy hot holes and migrated to the surface of further degradation. After being irradiated by NIR light for 150 min, the degradation rates of TC and CIP were 78.91% and 99.26% respectively. Lu et al. [22] prepared $\text{W}_{18}\text{O}_{49}/\text{ZnIn}_2\text{S}_4$ heterojunction by freeze-drying. $\text{W}_{18}\text{O}_{49}$ with free electrons had LSPR effect due to the restriction of W^{5+} - W^{5+} on surrounding local electrons, and the H_2 production rate was 902.57 μmol in 3 h under simulated sunlight, which was 449 times and 6.30 times those of $\text{W}_{18}\text{O}_{49}$ and ZnIn_2S_4 , respectively. Li et al. [23] obtained the $\text{Bi}_{19}\text{Br}_{3}\text{S}_{27}$ nanowires rich in Br-S double vacancies by alkaline etching. Because of the double LSPR effect caused by abundant Br and S double vacancies and Bi-O bonds introduced on the surface, it not only produced NIR light response, but also further hydrogenated ^{13}CO to methanol.

In addition, the electrons and holes stored in heterojunction could be released in the dark, and reacted with the dissolved oxygen to generate active species such as $\cdot\text{O}_2$, $\cdot\text{OH}$ and $^{1}\text{O}_2$, which continued to drive the dark catalytic reaction [24]. Yan et al. [25] prepared Z-scheme $\text{Bi}_4\text{TaO}_8\text{Cl}/\text{W}_{18}\text{O}_{49}$ heterojunction by solvothermal method. Under sunlight irradiation, a large number of photogenerated electrons could be stored in the oxygen vacancy defect of $\text{W}_{18}\text{O}_{49}$. When the light source was turned off, heating $\text{W}_{18}\text{O}_{49}$ could induce the release of stored electrons and excite them to the CB of $\text{Bi}_4\text{TaO}_8\text{Cl}$, so that the reduction reaction of CO_2 occurred in the dark, and the conversion efficiency of CO_2 was 23.42 $\mu\text{mol}\cdot\text{g}^{-1}\cdot\text{h}^{-1}$. Thus, the electrons stored in heterojunction could be released in the dark to drive the dark catalytic reaction [26].

However, all the heterojunctions with dark catalytic properties mentioned above released electrons stored by pre-illumination in the dark for reduction reaction, and the active species such as h^+ and $\cdot\text{OH}$ radicals rarely or even did not participate in the dark oxidation catalytic reaction. Wang et al. [27] enhanced the intrinsic polarization electric field of V_2C MXene by adjusting the surface end groups of the V_2C MXene crystal and weakening the degree of surface oxidation, so that it could store h^+ and e^- at the same time. The positive piezoelectric effect in dark light could directly release and store h^+ and e^- to degrade antibiotic pollutants. The degradation rate of V_2C to 40 $\text{mg}\cdot\text{L}^{-1}$ TC was 57.91%, and the removal rate of organic carbon was 23% after 140 min in the dark. Therefore, the intrinsic polarized electric field of the catalyst could be used to store electrons and holes, driving its piezoelectric catalytic reaction in the dark and all-weather energy storage piezoelectric catalysis. There are the polarized electric fields in both BiOBr and $\text{Bi}_x\text{O}_y\text{Br}_z$ crystals, and electrons and holes are stored in the crystals. Most of the studies on $\text{BiOBr}/\text{Bi}_x\text{O}_y\text{Br}_z$ attributed the enhancement

mechanism of the degradation ability of pollutants to the Z-scheme heterogeneity formed by the interface electric field, yet none of them have systematically investigated the influence of the interface electric field on the polarization field of $\text{BiOBr}/\text{Bi}_x\text{O}_y\text{Br}_z$ heterojunction crystals, nor have they studied the enhancement mechanism of pollutant degradation capability due to the polarization field-induced storage of electron-hole pairs in the crystals of BiOBr and $\text{Bi}_x\text{O}_y\text{Br}_z$.

In this study, by adjusting the pH of the precursor solution, different polymer ions of BiO^+ were formed, and the homogeneous nucleation hydrothermal crystallization was carried out to prepare energy storage $\text{BiOBr}@\text{Bi}_4\text{O}_5\text{Br}_2$ heterojunction piezoelectric catalysts. The formation mechanism of $\text{BiOBr}@\text{Bi}_4\text{O}_5\text{Br}_2$ heterojunction was studied, the regulation mechanism of the interfacial electric field on the polarized electric field of energy storage $\text{BiOBr}@\text{Bi}_4\text{O}_5\text{Br}_2$ heterojunction was explored, the mineralization paths of $\text{BiOBr}@\text{Bi}_4\text{O}_5\text{Br}_2$ heterojunction to TC and CIP in dark, visible light and NIR light were simulated, the enhancement mechanism of piezoelectric catalytic performance of energy storage $\text{BiOBr}@\text{Bi}_4\text{O}_5\text{Br}_2$ heterojunction was clarified, and the essence of enhancing catalytic activity of Z-scheme or S-scheme heterojunction at the interface was expanded, which provided a new idea for preparing around the clock energy storage piezoelectric catalytic materials from the traditional bismuth-based nanomaterials with the intrinsic polarized electric field.

2. Experimental section

2.1. Synthesis of $\text{BiOBr}@\text{Bi}_4\text{O}_5\text{Br}_2$

All the chemicals used were analytical grade reagents without further purification. 0.1 mol of $\text{Bi}(\text{NO}_3)_3\cdot 5\text{H}_2\text{O}$ was added into 40 mL of deionized water, 0.05 mol of NaBr was added while stirring, and stirred at room temperature for a proper time until a uniform solution was formed. The pH of the solution was adjusted with 1 $\text{mol}\cdot\text{L}^{-1}$ NaOH to make the pH of the precursor solution equal to 3, 6, 9, 12 and 14. Then, the precursor solution was transferred to a 100 mL tetrafluoroethylene-lined autoclave, heated at 160 °C for 12 h, and naturally cooled to room temperature. The precipitate was collected by centrifugation, washed several times with ethanol and deionized water, and finally dried in an oven at 60 °C for 6 h. According to the different pH values of the precursor solution, they were labeled as BOB (with unadjusted pH), BOB-3, BOB-6, BOB-9, BOB-12 and BOB-14 respectively.

2.2. Characterization

An X-ray diffractometer (XRD, BDX3300, $\text{Cu K}\alpha$, $\lambda=0.15406$ nm, 40 kV, 40 mA, 10 ~ 70, 8°/min) was used to analyze the phase composition and crystal structure of the samples. An X-ray photoelectron spectroscopy (XPS, Model XSAM800, Shimadzu-Kratos Ltd, Japan) was used to analyze the surface element composition and chemical state, and the obtained data were corrected by the characteristic peak of C 1 s at 284.6 eV. An Electron paramagnetic resonance (EPR, Bruker, A300) was used to characterize the defect structures and concentrations of the samples. A microscopic confocal laser Raman spectrometer (Raman, Renishawinvia, UK, Excitation wavelength: 532 nm, argon ion laser) was used to test the crystal structure of the samples. A field emission scanning electron microscope (FE-SEM, FEI Verios 460) and a (high resolution) transmission electron microscope (TEM(HRTEM), FEI-Tecnai, G2 F20) were used to observe the microstructure, phase composition and crystal structure of the samples. The ultraviolet-visible-near infrared diffuse reflectance spectra of the samples obtained by an ultraviolet-visible-near infrared spectrophotometer (UV-Vis-NIR DRS, DRS, Cray500, Agilent, U.S.A) were used to analyze the optical properties of the samples. A piezoelectric power microscope (PFM, Bruker Dimension Icon, Germany, excitation voltage: ± 10 V) was used to detect the deformation of the samples under the applied excitation voltage to study the surface potential and piezoelectric response of the materials

for PFM analysis. The surface potential mode of an Atomic Force Microscope (KPFM, Bruker Dimension Icon, Germany) was used to test the surface potential distribution of the samples. The obtained photoluminescence spectrum (PL, Edinburgh FS5 fluorescence spectrometer, excitation wavelength: 374 nm) and the time-resolved photoluminescence spectrum (TR-PL, Edinburgh FS5, excitation wavelength: 523 nm) were used to study the relaxation process of photogenerated carriers.

2.3. Dark catalytic experiment

The dark catalytic activity of the samples was evaluated by using mechanical stirring method and ultrasonic vibration method to degrade pollutants as model reactions in dark environment. 50 mg of catalysts were dispersed into 50 mL of 20 mg·L⁻¹ TC, 10 mg·L⁻¹ CIP, 20 mg·L⁻¹ BPA, 10 mg·L⁻¹ RhB, 10 mg·L⁻¹ MB and 10 mg·L⁻¹ MO solution, respectively. The mechanical stirring method was to put them in an XPA-7 photochemical reactor for magnetic stirring (1000 r·min⁻¹) and ultrasound. The concentrations of the residual pollutants in the supernatant were determined by a UV-Vis spectrophotometer (SP-756 P). After centrifugation, the absorbances of TC, CIP, BPA, RhB, MB and MO at λ =358 nm, 268 nm, 280 nm, 554 nm, 664 nm and 460 nm were measured respectively. The degradation rate of pollutants was calculated by the formula $\eta=1-(A_t/A_0) \times 100\%$, where η was the degradation rate; A_0 was the absorbance of the original pollutant solution; and A_t is the absorbance of the pollutant solution at any reaction time (t). The mineralization rate and decomposition products of pollutants were analyzed by determining the total organic carbon (TOC) and the liquid chromatography-tandem mass spectrometry (HPLC-MS HPLC chromatograph: Waters 2695, chromatographic column: C18 column 250 * 4.6 mm 3 μ m, MS mass spectrometer: Waters ZQ2000 MS).

2.4. Photocatalytic experiment

The full-spectrum photocatalytic activity of the sample was evaluated by using the visible light and NIR light degradation pollutants as model reactions. The reaction was conducted under the irradiation conditions of visible light (a 500 W xenon lamp, UVREF400, 400–800 nm) and NIR light (a 500 W xenon lamp, QFS2500+800 nm long-pass filter, 800–2500 nm) respectively, and other operation processes were the same as dark catalytic reaction.

2.5. Photoelectrochemical experiment

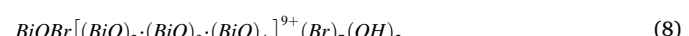
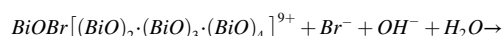
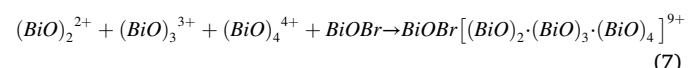
The photoelectrochemical test was carried out on a standard three-electrode chemical workstation (CHI660E) with a platinum sheet as the counter electrode, KCl saturated Ag/AgCl electrode as the reference electrode and the sample preparation as the working electrode. Preparation of working electrode was as follows. 0.02 g catalyst was added to the mixed solution of 1 mL ethanol and 0.2 mL film-forming reagent. After ultrasonic dispersion for 30 min, a uniform suspension was obtained. The suspension was dispersed on the activated FTO glass, annealed at 200 °C for 2 h, and naturally cooled to room temperature to obtain the working electrode. The test light source was a 500 W xenon lamp, and the visible light and NIR light source was realized by configuring appropriate filters. Using 0.1 mol·L⁻¹ Na₂SO₄ solution as electrolyte, the transient optical flow response (i-t) and electrochemical impedance (EIS) spectra of the samples were tested.

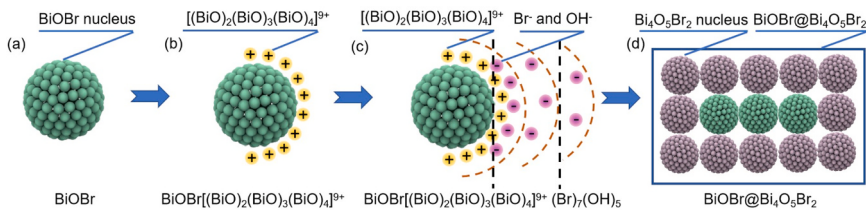
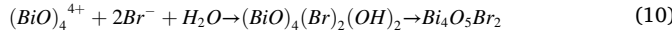
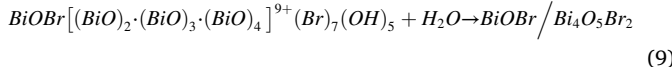
3. Results and discussion

3.1. Formation mechanism of energy storage BiOBr@Bi₄O₅Br₂ heterojunction

The homogeneous nucleation process of the BiOBr@Bi₄O₅Br₂ heterojunction is as follows: Bi(NO₃)₃·5 H₂O is dissolved in water and

hydrolyzed to form BiO⁺ (Eq. 1), and NaBr is hydrolyzed to Br⁻ and Na⁺ (Eq. 2). When stirred at room temperature, BiO⁺ and Br⁻ in aqueous solution form BiOBr nuclei (Eq. 3). When the pH value is less than 3, BiO⁺ and Br⁻ continuously aggregate into the crystal nuclei of BiOBr (Fig. S3a), and hydrothermal formed BiOBr crystals (Fig. S1-S2). When NaOH solution is added to adjust the pH value of the precursor solution to 3–9, BiO⁺ and Br⁻ quickly form BiOBr crystal nuclei in the solution, and the crystal nuclei grow into a nano-flake structure. BiO⁺ without crystal nuclei in the aqueous solution will gradually form dimer ions (BiO)₂²⁺, trimer ions (BiO)₃³⁺ and tetramer ions (BiO)₄⁴⁺ (Eqs. 4–6). These polymer ions are uniformly adsorbed on the surface of the crystal nucleus of the BiOBr nanosheet to form an adsorption layer, which constitutes the BiOBr[(BiO)₂(BiO)₃(BiO)₄]⁹⁺ colloidal particles (Eq. 7 and Fig. 1b). The colloidal particles are positively charged, and then they will adsorb Br⁻ and OH⁻ in the solution, forming a diffusion electric double layer and forming the BiOBr[(BiO)₂•(BiO)₃•(BiO)₄]Br₇(OH)₅ micelles (Eq. 8 and Fig. 1c). The saturated crystallization occurs in the hydrothermal high temperature reaction system (Eq. 9), and the micelles form BiOBr crystals (Fig. S1 and Fig. S2d-f). In the process of forming the diffusion electric double layer, an interfacial electric field is formed between BiOBr and [(BiO)₂•(BiO)₃•(BiO)₄]⁹⁺ at the solid-liquid interface of the colloidal particles, and the direction points to BiOBr, thus forming the BiOBr@Bi₄O₅Br₂ heterojunction wrapped with Bi₄O₅Br₂ on the surface of the BiOBr nanosheets (Fig. 1d). The competition between BiOBr and Bi₄O₅Br₂ is formed due to the existence of BiO⁺ in the solution, which leads to the thinning of nanoplatelets of the BiOBr@Bi₄O₅Br₂ heterojunction (Fig. S3b, Fig. S3d-f). When pH=12, all BiO⁺ in the reaction system polymerize to form tetramer (BiO)₄⁴⁺ ions, and (BiO)₄⁴⁺ and Br⁻ form (BiO)₄Br₂(OH)₂, which is saturated and crystallized in the hydrothermal high-temperature reaction system to form the nano-flaky Bi₄O₅Br₂ crystals (Eq. 10 and Fig. S3c). When pH=14, BiO⁺ exists as (BiO)_nⁿ⁺, and forms amorphous (BiO)_n(OH)_n with high concentration of OH⁻, and the (BiO)_n(OH)_n undergoes hydrothermal reaction at 160 °C for 12 h to form tetragonal Bi₂O₃ (Eqs. 11–13). When different polymer ions of BiO⁺ are formed by adjusting the pH of the precursor solution, if pH<3, BiOBr crystals are formed by hydrothermal method; if pH=3–9, BiOBr@Bi₄O₅Br₂ crystals are formed by homogeneous nucleation hydrothermal method; if pH=12, Bi₄O₅Br₂ crystals are formed by hydrothermal method; and if pH=14, tetragonal Bi₂O₃ crystals are formed by hydrothermal method. These show that the BiOBr@Bi₄O₅Br₂ heterojunction formed by regulating the precursor solution with pH=3–9 has the ability to degrade many pollutants in the dark and has a broad spectrum. A detailed comparison is available in the Supporting Information (Table S1).



Fig. 1. Formation process of the BiOBr@Bi₄O₅Br₂ heterojunction.

The XPS diagram of the BiOBr@Bi₄O₅Br₂ heterojunction can be seen that BOB, BOB-6 and BOB-12 contain elements of Bi, O and Br, while BOB-14 only contains elements of Bi and O (Fig. S5a), which is consistent with the XRD results (Fig. S1). The O 1 s spectrum of BOB (Fig. S5b) can be fitted into two peaks, which corresponds to oxygen vacancy and lattice oxygen atom of the [Bi₂O₂]²⁺ layer at 532.48 eV and 530.28 eV, respectively, and the oxygen vacancy concentration is about 10.44%. The O 1 s spectrum of BOB-12 can be fitted into two peaks, which corresponds to oxygen vacancy and lattice oxygen atom of the [Bi₂O₂]²⁺ layer at 532.28 eV and 529.68 eV, respectively, and the concentration of oxygen vacancy is about 3.84%. The O 1 s spectrum of BOB-6 can be fitted into two peaks, which corresponds to oxygen vacancy and lattice oxygen atom of the [Bi₂O₂]²⁺ layer at 531.18 eV and 528.78 eV, respectively, and the oxygen vacancy concentration is about 14.46%. Compared with BiOBr and Bi₄O₅Br₂, the oxygen vacancy concentration is increased, and the binding energy is shifted to the right, which proves that the charge density of O of Bi₄O₅Br₂ in BiOBr@Bi₄O₅Br₂ is increased. The O 1 s spectrum of BOB-14 can also be fitted as two peaks, which corresponds to oxygen vacancies and lattice oxygen atoms of the [Bi₂O₂]²⁺ layer at 531.78 eV and 529.98 eV, respectively, and the concentration of oxygen vacancy is about 3.85%.

In the Bi 4 f spectrum (Fig. S5c), BOB has two strong peaks around ~164 eV and ~158 eV, which belong to Bi³⁺ 4 f_{7/2} and Bi³⁺ 4 f_{5/2}, respectively. After fitting, it can be divided into four binding energies: 163.48 eV and 158.18 eV, 162.28 eV and 156.98 eV. 163.48 eV and 158.18 eV belonging to Bi³⁺, and the concentration of Bi³⁺ is about 63.03%. The low binding energy at 162.28 eV and 156.98 eV may be attributed to the low charge Bi ions (Bi^{+(3-x)}) in the compound, and the concentration of Bi^{+(3-x)} is about 36.97%. Since oxygen vacancy in BiOBr crystals bound a large number of local electrons, which were combined with Bi³⁺ ions to form low-priced Bi^{+(3-x)} ions, forming Bi^{+(3-x)} doped BiOBr crystals, and a negative charge center and acceptor energy level at the top of the valence band (VB) of BiOBr crystals, where a hole was bound by Bi^{+(3-x)}. That is, both electrons and holes could be stored in the BiOBr crystal. Bi 4 f spectrum of BOB-12 can also be divided into 161.88 eV and 156.48 eV (Bi³⁺), 160.68 eV and 155.28 eV (Bi^{+(3-x)}) by fitting. The concentration of Bi³⁺ is about 70.28% and that of Bi^{+(3-x)} is about 29.72%. Therefore, electrons and holes can also be stored in the Bi₄O₅Br₂ crystal. BOB-6 can also be fitted into 162.08 eV and 156.78 eV (Bi³⁺), 160.58 eV and 155.28 eV (Bi^{+(3-x)}), with the concentration of Bi³⁺ being about 60.93% and that of Bi^{+(3-x)} being about 39.07%. Bi^{+(3-x)} is doped with both BiOBr and Bi₄O₅Br₂ crystals. Due to the existence of the diffusion electric double layer, an interfacial electric field is formed between BiOBr and [(BiO)₂•(BiO)₃•(BiO)₄]⁹⁺ at

the solid-liquid interface of the colloidal particles. When the BiOBr@Bi₄O₅Br₂ heterojunction is formed, the surface of the BiOBr crystal is wrapped by Bi₄O₅Br₂, and when hydrothermal crystallization occurs, BiOBr forms OVs. Electrons bound by the BiOBr intrinsic polarization electric field migrate to Bi₄O₅Br₂ under the action of the interfacial electric field, which increases the Bi³⁺ concentration of BiOBr and the Bi^{+(3-x)} concentration of Bi₄O₅Br₂. Under the action of the intrinsic polarization electric field and the interface electric field, Bi₄O₅Br₂ stores h⁺ and BiOBr stores e⁻ in the BiOBr@Bi₄O₅Br₂ heterojunction. BOB-12 has two strong peaks around ~161.38 eV and ~156.88 eV, which belongs to Bi³⁺. In the Br 3d spectrum (Fig. S5d), the characteristic peaks of BOB at 69.88 and 68.08 eV correspond to Br 3d_{3/2} and Br 3d_{5/2}, respectively [28], and the Br 3d (69.88 and 68.08 eV) of BOB-6 and Br 3d (69.48 and 68.18 eV) of BOB-12 has lower binding energy than that of BOB, which indicates that the charge density of Br element is increased, which is caused by the transfer of electron free carriers bound by BiOBr to Bi₄O₅Br₂ under the action of the interfacial electric field.

The above charge transfer behavior is further verified by the interface differential charge density. The green and yellow areas in the interface differential charge density diagram of BiOBr@Bi₄O₅Br₂ represent charge accumulation and charge consumption respectively (Fig. S5e). At the interface of BiOBr@Bi₄O₅Br₂, electrons accumulate to form an electron-rich region on the BiOBr side and a hole-rich region on the Bi₄O₅Br₂ side. At the interface of BiOBr@Bi₄O₅Br₂, the interface electric field at the interface of Bi₄O₅Br₂ pointed to BiOBr is formed. The phenomenon of charge accumulation or consumption also appears on O atoms of BiOBr and Bi₄O₅Br₂, which proves that the formation of the interfacial electric field changes the electron distribution in the crystals, and the uneven charge distribution changes the intensity of the polarized electric field, which changes the intrinsic polarized electric field in the BiOBr and Bi₄O₅Br₂ crystals. In the EPR spectrum (Fig. S5f), all BOB, BOB-6 and BOB-12 show characteristic signal peaks belonging to oxygen vacancies at g=2.0037 [29], and the EPR signals of BOB-6 are obviously stronger than those of BOB and BOB-12, indicating that the defect concentration in BOB-6 crystal is the largest. The above test results prove that the interface electric field of Bi₄O₅Br₂ pointing to BiOBr is formed in the generated BiOBr@Bi₄O₅Br₂ heterojunction. Under the action of the interface electric field, the electrons bound by BiOBr migrate to Bi₄O₅Br₂, which changes the electron distribution in the crystal, and the uneven charge distribution tends to change the polarization electric field intensity.

In addition, the separation and transport efficiency of carriers have a great influence on the performance of the catalyst. As a dynamic driving force, the strong IEF can promote the better separation of hole-electron pairs. According to Gouy-Chapman formula (S5-S9), the IEF intensity (F_s) of the catalyst can be calculated by the surface potential and the Zeta potential. The surface potential diagram of the sample is measured by Kelvin probe force microscope (KPFM) (Fig. 2a-c). The two-dimensional field of surface potential distributions are obviously different among samples, but there are relatively uniform among samples (Fig. 2d-f). In Fig. 2d-f, the red lines are the positions of the surface potential curves (V) in the test. According to V, the average surface potential (V_s) of the catalyst at the position of the red lines are calculated. The average surface potentials (V_s) of BOB, BOB-6 and BOB-12 are 885.52, 961.78 and 1021.98 mV, respectively (Fig. 2g). The Zeta

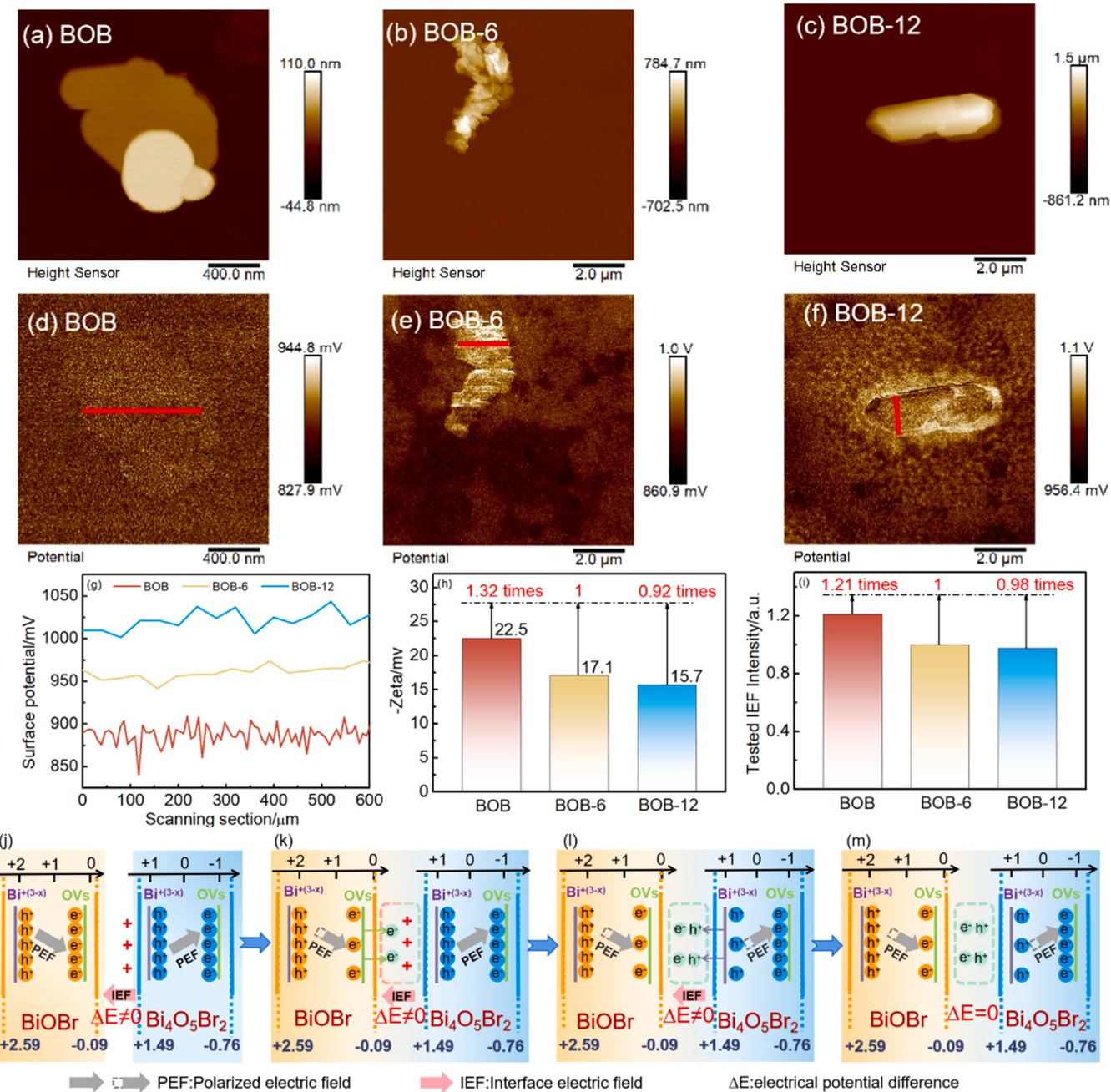


Fig. 2. Surface topography of (a) BOB, (b) BOB-6 and (c) BOB-12; KPFM diagrams of (d) BOB, (e) BOB-6 and (f) BOB-12; (g) the surface potential curves of BOB, BOB-6 and BOB-12 along the line in Fig. 2d-f; (h) the zeta potential values and (i) the electric field strengths (assuming that the strength of BOB-6 was “1”); (j-m) The process of storing electron holes in energy storage BiOBr@Bi₄O₅Br₂ crystal.

potentials (ζ) of BOB, BOB-6 and BOB-12 are -22.5 , -17.1 and -15.7 mV, respectively (Fig. 2h). Finally, after calculation, it is found that the IEF strengths ($\frac{F_{s1}}{F_{s2}}$) of BOB-6 are 1.21 times and 0.98 times those of BOB and BOB-12, respectively (Fig. 2i). (The related discussion is in Supporting Information). [8,30] In order to study the influence of polarization electric field on the energy band structure of heterojunction, the optical characteristics of the sample are characterized by UV-Vis-NIR diffuse reflection spectrum. As shown in Fig. S4a, the light absorption edges of BOB and BOB-12 are 437.29 nm and 472.63 nm, respectively. The formula for calculating the optical band gap of the photocatalyst is: $a(hv) = A(hv - Eg)^{\frac{n}{2}}$, where α , h , v and A are absorption coefficient, Planck constant, optical frequency and proportionality constant, respectively. The value of n depends on the characteristics of

semiconductor transition. For the Bi-based photocatalyst, it corresponds to indirect transition, and n is equal to 4. The band gap of indirect transition makes the emission of excited electrons to valence band with the help of phonons, thus prolonging the service life of electron-hole pairs and improving photocatalytic activity. According to Kubelka-Munk conversion, it was calculated that the band gap energy of BiOBr is about 2.68 eV, and that of Bi₄O₅Br₂ is about 2.25 eV (Fig. S4b). According to the XPS-VB spectrograms of Fig. S4c-d, it can be concluded that the VB of BiOBr is 2.59 eV, and that of Bi₄O₅Br₂ is 1.49 eV. According to the formula: $E_{CB} = E_{VB} - Eg$, the CB of BiOBr is -0.09 eV and that of Bi₄O₅Br₂ is -0.76 eV. Because the homogeneous nucleation hydrothermal method forms the BiOBr@Bi₄O₅Br₂ heterojunction, the energy band at the heterojunction interface does not bend. [31] Through

the above tests, the regulation mechanism of interfacial electric field on polarized electric field of energy storage $\text{BiOBr}@\text{Bi}_4\text{O}_5\text{Br}_2$ heterojunction is put forward. In the process of forming the diffusion electric double layer, the interfacial electric field (IEF) is formed at the solid-liquid interface of BiOBr and $\text{Bi}_4\text{O}_5\text{Br}_2$ colloidal particles, and $\Delta E=0$ (the red arrow in Fig. 2j), and the direction of the intrinsic polarization electric field in BiOBr and $\text{Bi}_4\text{O}_5\text{Br}_2$ crystals is deviated (the black arrow in Fig. 2j). Under the action of the interface electric field, some electrons stored in the BiOBr crystal migrate to the interface (green electrons in Fig. 2k), and some electrons remain near the oxygen vacancy at the bottom of the CB of BiOBr (the yellow electrons in Fig. 2k), so the intrinsic polarization electric field in the crystal will be reduced (the dotted line in the black arrow in Fig. 2k), and some electrons stored in the BiOBr crystal migrate to the interface which will cause the interface electric field to change. It also induces some holes stored above the VB in the $\text{Bi}_4\text{O}_5\text{Br}_2$ crystal to migrate to the interface (the green holes in Fig. 2l), and some holes remain near $\text{Bi}^{+(3-x)}$ above the VB in $\text{Bi}_4\text{O}_5\text{Br}_2$ crystal (the blue holes in Fig. 2l), and the intrinsic polarization electric field of $\text{Bi}_4\text{O}_5\text{Br}_2$ crystal will be reduced (the dotted line in the black arrow in Fig. 2l). Under that action of coulomb force, the electrons of BiOBr and the hole of $\text{Bi}_4\text{O}_5\text{Br}_2$ migrating to the interface attract each other, forming the positive and negative charge regions and the e^-h^+ exciton, so that the interface potential is shown to be zero, $\Delta E=0$, which leads the intrinsic polarization electric field of BiOBr and the intrinsic polarization electric field of $\text{Bi}_4\text{O}_5\text{Br}_2$ to form a series polarization electric field of $\text{BiOBr}@\text{Bi}_4\text{O}_5\text{Br}_2$ heterojunction. A series polarized electric fields cause holes in heterojunction to be stored in the BiOBr crystal, electrons to be stored in the $\text{Bi}_4\text{O}_5\text{Br}_2$ crystal, and excitons to be stored in the interface (Fig. 2m). When the heterojunction is static, the intrinsic polarization electric fields will be lower than or the same as those of the BiOBr crystal and the $\text{Bi}_4\text{O}_5\text{Br}_2$ crystal.

Fig. 3 is the PFM diagram of the $\text{BiOBr}@\text{Bi}_4\text{O}_5\text{Br}_2$ heterojunction. In contact mode, when the conductive cantilever with 10 V AC voltage is

swept across the surface of the sample, it tends to expand and contract in different degrees due to the inverse piezoelectric effect. After applying a deflection voltage of 10 V, the phase angle is reversed by about 180. Under the action of 10 V electric field, the amplitude-voltage curves of all BOB, BOB-6 and BOB-12 show a typical “butterfly ring” (Fig. 3a-c), resulting in the strain-electric field lag phenomenon. [32,33] This also proves that all BOB, BOB-6 and BOB-12 have the piezoelectric effect, and there is an intrinsic polarized electric field in the crystal, which is consistent with the KPFM results in Fig. 2. The asymmetry of piezoelectric “butterfly ring” is caused by the action of the piezoelectric field on the cantilever tip and the motion of the dipole. [34,35] The d_{33} of BOB, BOB-6 and BOB-12 are calculated by the piezoelectric butterfly ring fitting, which are $3.66 \text{ nm}\cdot\text{V}^{-1}$, $6.29 \text{ nm}\cdot\text{V}^{-1}$ and $5.07 \text{ nm}\cdot\text{V}^{-1}$, respectively. The interfacial electric field of the BOB-6 heterojunction changes the intrinsic polarization electric field in the BiOBr crystal and the $\text{Bi}_4\text{O}_5\text{Br}_2$ crystal, which enhances the piezoelectric effect of the energy storage $\text{BiOBr}@\text{Bi}_4\text{O}_5\text{Br}_2$ heterojunction.

According to the UV-vis spectra of MB decolorization experiment by $\text{BiOBr}@\text{Bi}_4\text{O}_5\text{Br}_2$ in the dark (Fig. 4a-c), it can be calculated that the e^- concentrations stored by BOB, BOB-6 and BOB-12 are $46.39 \mu\text{mol}\cdot\text{g}^{-1}$, $94.23 \mu\text{mol}\cdot\text{g}^{-1}$ and $40.36 \mu\text{mol}\cdot\text{g}^{-1}$, respectively, and the electron concentrations of BOB-3, BOB-9 and BOB-14 are listed in Supporting Information (Fig. S6a-c). Using an electron spin resonance spectroscopy (EPR), the h^+ concentrations released by BOB, BOB-6 and BOB-12 within 10 min are calculated to be $65.41 \mu\text{mol}\cdot\text{g}^{-1}$, $86.17 \mu\text{mol}\cdot\text{g}^{-1}$ and $64.37 \mu\text{mol}\cdot\text{g}^{-1}$, respectively [36]. MB decolorization experiment and TEMPO- h^+ EPR test prove that the intrinsic polarization electric fields in BOB, BOB-6 and BOB-12 crystals lead to the simultaneous storage of electrons and holes in the crystals. The concentrations of electrons and holes stored in the $\text{BiOBr}@\text{Bi}_4\text{O}_5\text{Br}_2$ heterojunction are higher than those in the BiOBr and $\text{Bi}_4\text{O}_5\text{Br}_2$ crystals, and the $\text{BiOBr}@\text{Bi}_4\text{O}_5\text{Br}_2$ heterojunction is an energy storage $\text{BiOBr}@\text{Bi}_4\text{O}_5\text{Br}_2$ heterojunction. Different polymer ions of BiO^+ are formed by adjusting

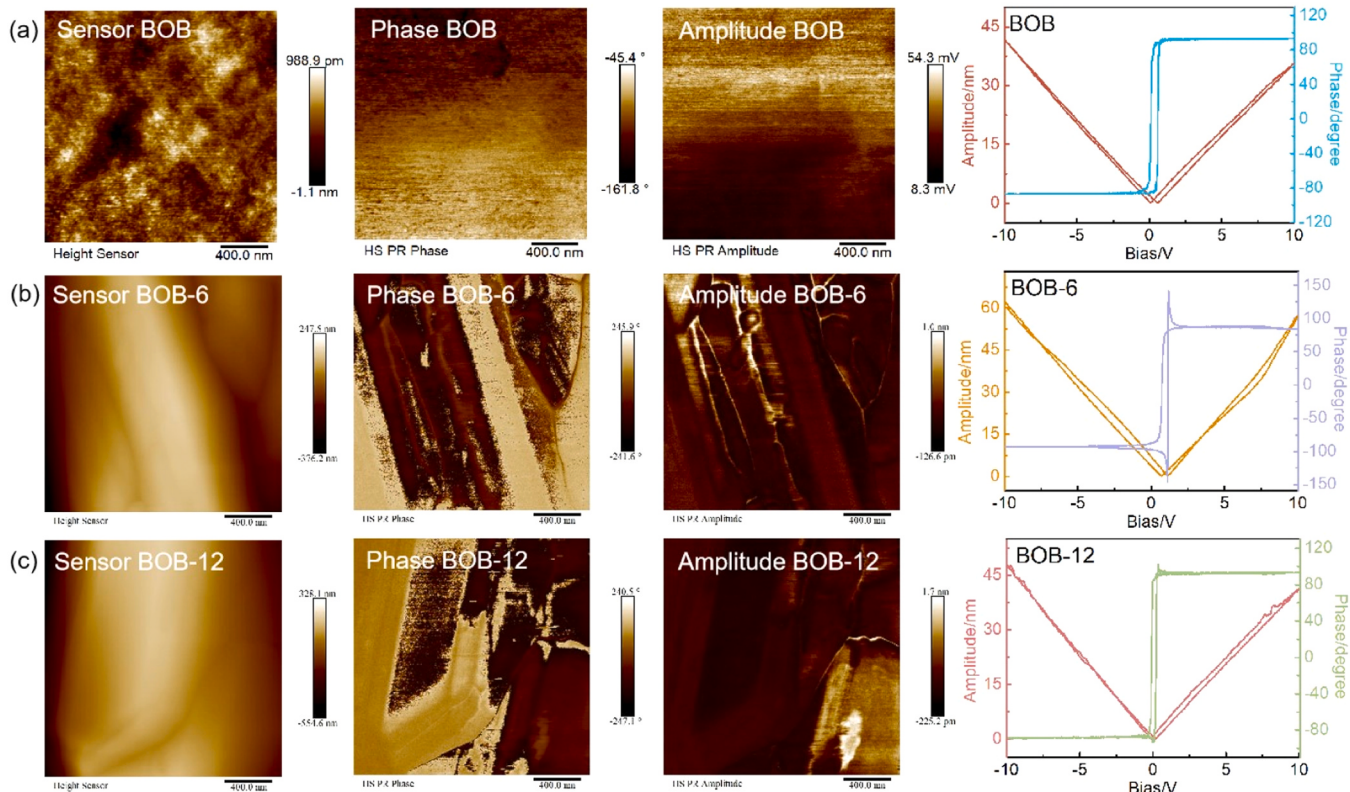


Fig. 3. PFM images of the $\text{BiOBr}@\text{Bi}_4\text{O}_5\text{Br}_2$ crystal: Surface topography, phase and amplitude topography and corresponding phase offset and amplitude-voltage curves of (a) BOB, (b) BOB-6, (c) BOB-12.

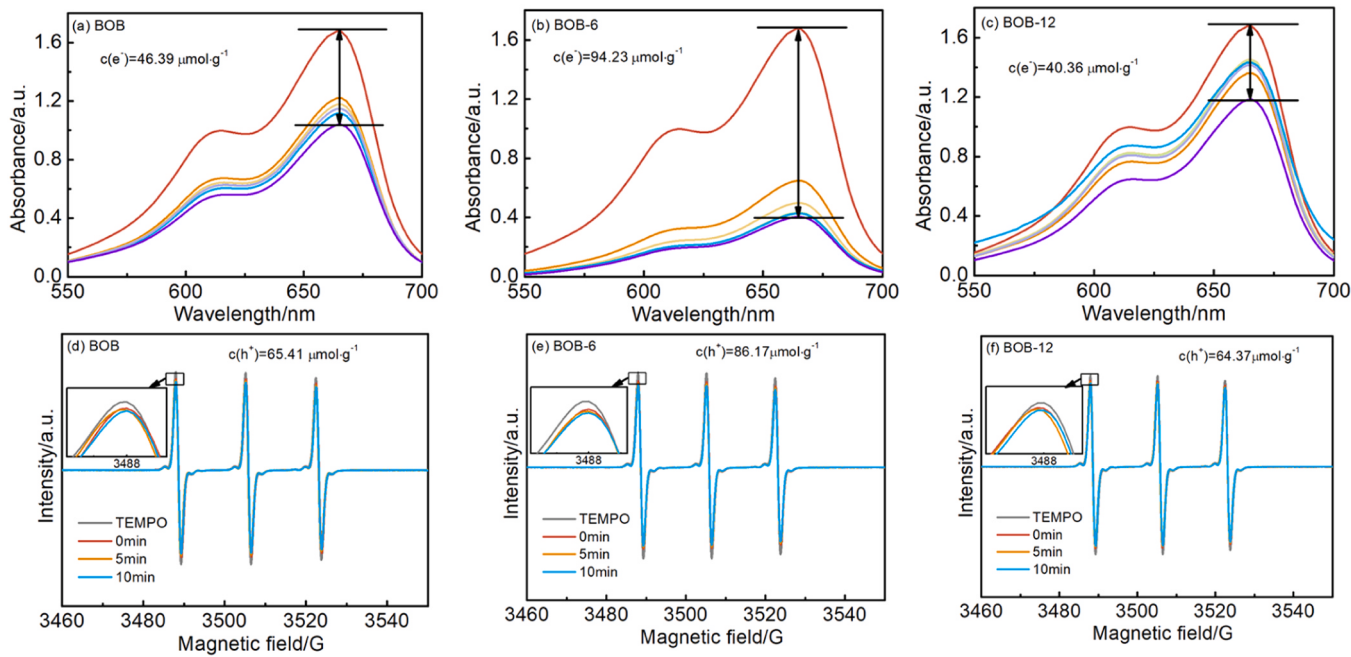


Fig. 4. In the dark: the stored electron concentrations of (a) BOB, (b) BOB-6 and (c) BOB-12 obtained by MB de-colorization experiments; TEMPO- h^+ EPR spectra of (d) BOB, (e) BOB-6 and (f) BOB-12 in dark.

the pH of the precursor solution, and different concentrations of electrons and holes can be stored in the energy storage $\text{BiOBr}@\text{Bi}_4\text{O}_5\text{Br}_2$ heterojunction. Therefore, the prepared energy storage $\text{BiOBr}@\text{Bi}_4\text{O}_5\text{Br}_2$ heterojunction formed by regulating the pH of the precursor solution has a recyclable storage mechanism of electrons, holes and excitons.

3.2. Dark catalytic performance

The dark catalytic activity of the catalyst is evaluated by degrading

pollutants in the dark by mechanical stirring. After mechanical stirring for 25 min in the dark, the degradation rates of $10 \text{ mg}\cdot\text{L}^{-1}$ CIP by BOB, BOB-3, BOB-6, BOB-9, BOB-12 and BOB-14 are 56.42%, 63.56%, 75.95%, 60.37%, 45.69% and 26.14%, respectively (Fig. 5a), and the TOC removal rate of CIP by BOB-6 reaches 44.52% (the inset in Fig. 5a). When mechanically stirred in the dark for 50 min, the degradation rates of $20 \text{ mg}\cdot\text{L}^{-1}$ TC by BOB, BOB-3, BOB-6, BOB-9, BOB-12 and BOB-14 are 32.93%, 57.12%, 63.44%, 47.69%, 40.52% and 24.35%, respectively (Fig. 5b). The TOC removal rate of TC by BOB-6 is 57.72% (the inset in Fig. 5b). In addition, the degradation rates of $20 \text{ mg}\cdot\text{L}^{-1}$ BPA, $10 \text{ mg}\cdot\text{L}^{-1}$

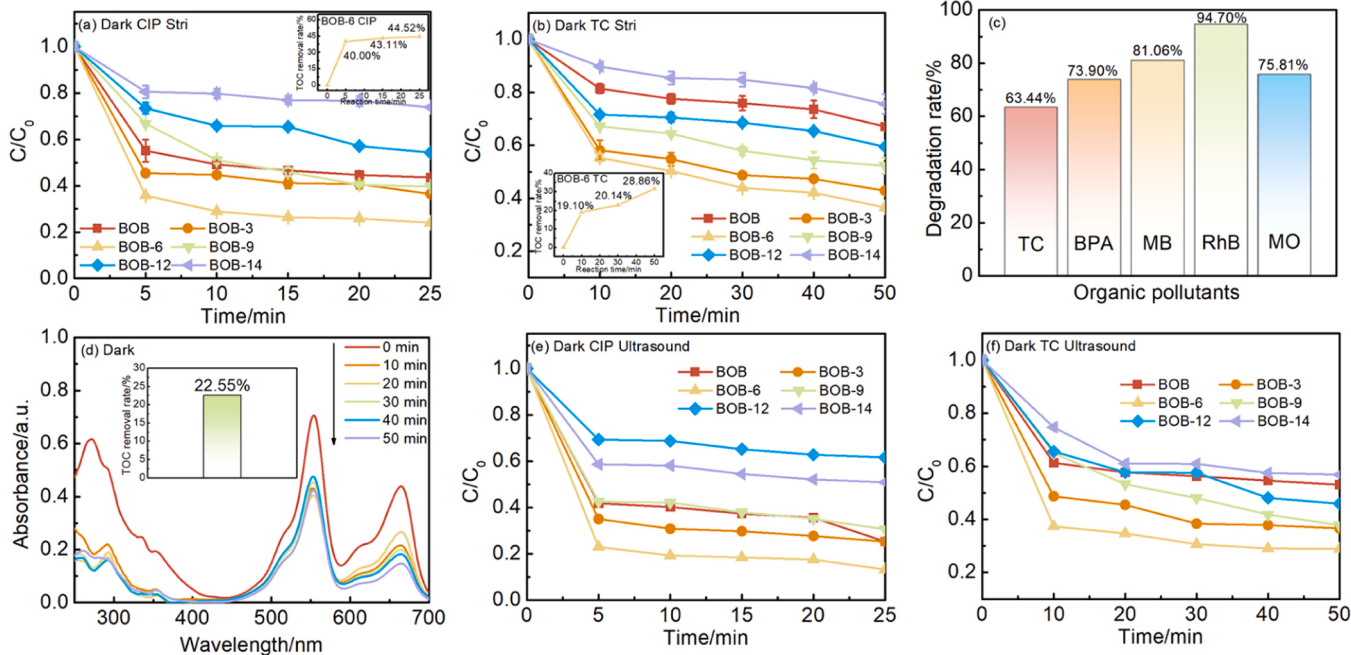


Fig. 5. Degradation performance of the energy storage $\text{BiOBr}@\text{Bi}_4\text{O}_5\text{Br}_2$ heterojunction in the dark: Under mechanical stirring, degradation activity of (a) CIP and (b) TC; (c) degradation experiment of other pollutants; and (d) the absorbance diagram of the UV-vis spectrogram of the mixed solution. Under ultrasonic vibration, degradation activity of (e) CIP and (f) TC.

MB, 10 mg·L⁻¹ RhB and 10 mg·L⁻¹ MO are 73.90%, 81.06%, 94.70% and 75.81%, respectively by BOB-6 after mechanically stirring for 50 min in the dark (Fig. 5c). The absorption bands of the mixed solution of 10 mg·L⁻¹ CIP, 20 mg·L⁻¹ TC, 10 mg·L⁻¹ MB and 10 mg·L⁻¹ RhB by BOB-6 are gradually weakened with the extension of degradation time (Fig. 5d), and the TOC removal rate of the mixed solution of 50 min in the dark is 22.55% (the inset in Fig. 5d), which shows that the BiOBr@Bi₄O₅Br₂ heterojunction has the ability to degrade many pollutants in the dark and has a broad spectrum. A detailed comparison is available in the Supporting Information (Table S1). Fig. S8 is the N₂ adsorption/desorption isotherm and the pore size distribution curve of BiOBr@Bi₄O₅Br₂ heterojunction. The existence of Type IV hysteresis loop proves that all samples show the obvious mesoporous characteristics (Fig. S8a). The BET specific surface areas of BOB (1.0025 cm²·g⁻¹) and BOB-12 (4.2492 cm²·g⁻¹) are smaller than that of BOB-6 (13.0520 cm²·g⁻¹). In addition, the total pore volume and the average pore diameter of BOB-6 are larger than those of BOB and BOB-12 (Fig. S8b and Table S4). Therefore, BOB-6 has a larger specific surface area, a pore volume and a pore size, and can provide larger adsorption and active sites, which are beneficial to the subsequent catalytic reaction.

In order to further illustrate the effect of the catalyst specific surface area on catalytic activity, ultrasonic vibration method is used to degrade the pollutants in the dark and the effect of the specific surface area of the catalyst on the catalytic activity is evaluated. After ultrasonic vibration for 25 min in the dark, the degradation rates of 10 mg·L⁻¹ CIP by BOB,

BOB-3, BOB-6, BOB-9, BOB-12 and BOB-14 are 74.71%, 74.77%, 86.78%, 69.45%, 38.4% and 49.12%, respectively (Fig. 5e). After ultrasonic vibration for 25 min in the dark, the degradation rates of 20 mg·L⁻¹ TC by BOB, BOB-3, BOB-6, BOB-9, BOB-12 and BOB-14 are 46.94%, 63.37%, 71.11%, 62.2%, 54.11% and 43.14%, respectively (Fig. 5f). It is proved that the energy storage BiOBr@Bi₄O₅Br₂ heterojunction can directly degrade antibiotics in the dark, and the energy storage BiOBr@Bi₄O₅Br₂ heterojunction has better degradation performance of antibiotics under dark and ultrasonic vibration. [37] Ultrasonic vibration can eliminate the adsorption effect caused by the increase of the specific surface area, which shows that the dark piezoelectric catalysis of the energy storage BiOBr@Bi₄O₅Br₂ heterojunction plays an important role in the dark, and the increase of the specific surface area has small effects on the dark piezoelectric catalysis activity.

The degradation process of CIP by BOB-6 in the dark is analyzed by LC-MS (Fig. S9, Fig. S10 and Table S3). BOB-6 degrades CIP into P17(*m/z*=167), P18(*m/z*=114), P19(*m/z*=98), P20(*m/z*=74) and P21(*m/z*=60), [38] which are finally converted into CO₂ and H₂O (Fig. S10). BOB-6 degrades TC into P20(*m/z*=174), P21(*m/z*=155), P22 (*m/z*=123), P23(*m/z*=102) to P24(*m/z*=60), [39] and then mineralizes into H₂O and CO₂ (Fig. S12, Fig. S13, Fig. S14 and Table S4). It is proved that the degradations of CIP and TC by the energy storage BiOBr@Bi₄O₅Br₂ heterojunction in the dark are the results of catalytic mineralization, not adsorption.

In the experiment of ten cycles of degradation of TC by BOB-6 in the dark (Fig. 6a), the degradation rate of TC by BOB-6 in the first cycle is

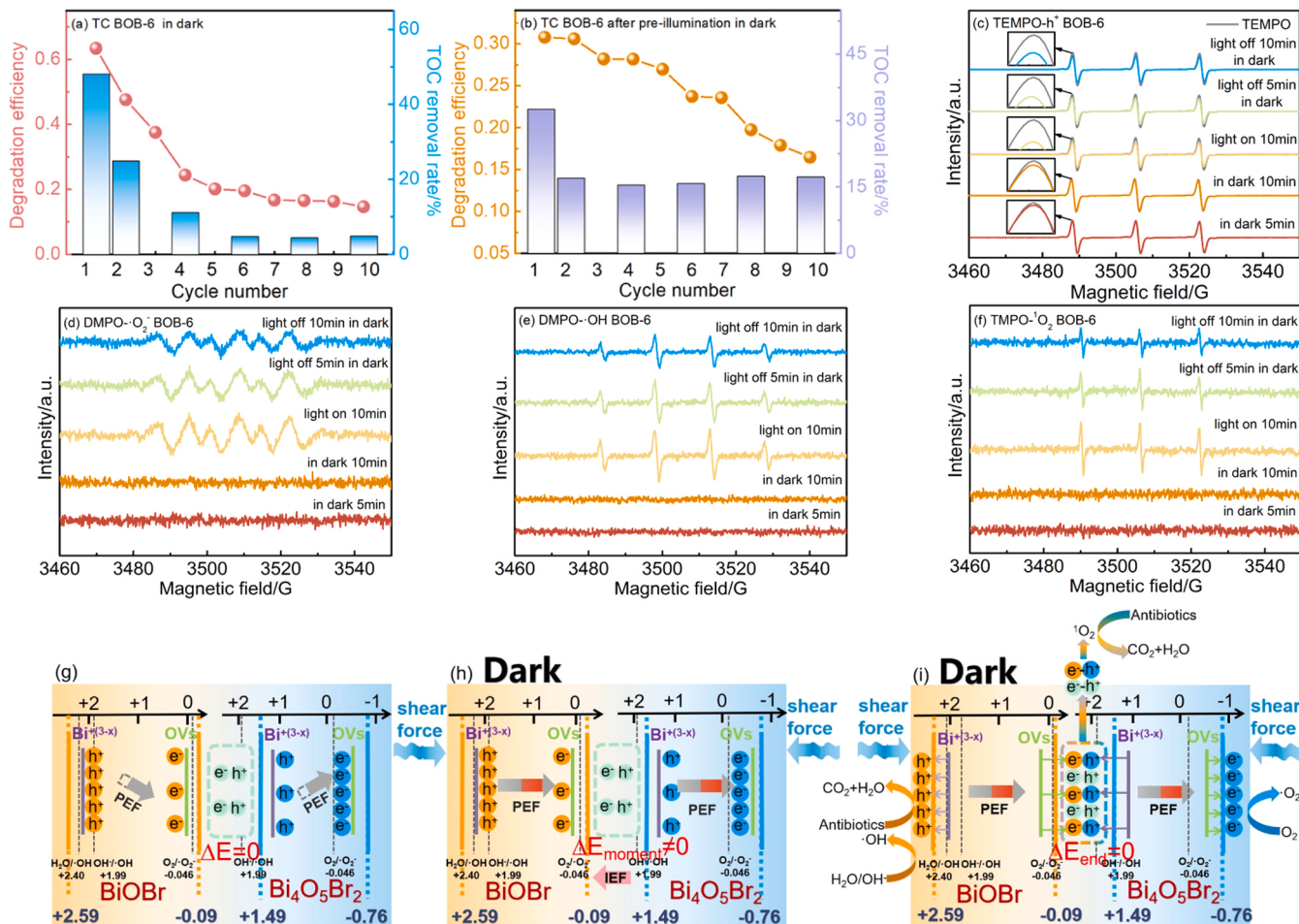


Fig. 6. (a) Degradation cycle experiment of TC by BOB-6 in the dark, and (b) degradation cycle experiment of TC by BOB-6 in the dark again after re-illumination for 30 min; EPR spectra of the energy storage BiOBr@Bi₄O₅Br₂ heterojunction in dark, re-illumination and re-darkness: (c) TEMPO-h⁺, (d) DMPO-O₂⁻, (e) DMPO-OH, (f) TMPO-O₂⁻. In the dark, the piezoelectric catalytic process of the energy storage BiOBr@Bi₄O₅Br₂ heterojunction: (g) energy storage heterojunction, (h) mechanical force to enhance polarized electric field, and (i) migration of the polarized electric field to release the stored electron holes.

63.44%, and the degradation rate remains stable at 15% after ten cycles, and the TOC removal rate of TC remains stable at around 15% from 48.06%. After the powder subjected to ten dark cycles is centrifuged and irradiated for 30 min, the dark cycle reaction is continued. The degradation rate of TC and TOC recovers to 30.79% and 32.55% for the first time, and after ten cycles, the degradation rate of TC and TOC is basically stable at about 15% (Fig. 6b), which is attributed to the gradual consumption of the stored electrons and holes. BOB-6 consumes electrons and holes stored in the preparation process in ten dark cycles. After being irradiated by visible light, the photogenerated electrons and holes can be stored in the heterojunction, which can be released again in the dark to continue to degrade TC. The XRD patterns before and after the cyclic degradation for ten times and after the cyclic degradation for ten times after being irradiated remain unchanged (Fig. S15). Therefore, the energy storage BiOBr@Bi₄O₅Br₂ heterojunction has good cycle stability and repairability in the dark.

In the dark for 5 min and 10 min, BOB-6 shows the obvious h⁺ characteristic peak signal, and after the light is turned off for 10 min, BOB-6 shows the h⁺ characteristic peak signal in the dark (Fig. 6c). EPR tests BOB-6 samples in the dark for 5 min and 10 min, and the characteristic peak signals of ·O₂, ·OH and ¹O₂ are not observed, but the characteristic peak signals of DMPO-·O₂, DMPO-·OH and TMPO-¹O₂ can be detected under the illumination for 10 min [40]. After turning off the illumination, the characteristic peak signals of DMPO-·O₂, DMPO-·OH and TMPO-¹O₂ can be detected again in the dark, and are gradually decreased with the extension of the dark time (Fig. 6d-f). The EPR test also proves that the energy storage BiOBr@Bi₄O₅Br₂ heterojunction has a good dark cycle repair. Through calculation, it can be known that the hole concentration stored again after irradiation of BOB-6 is 221.76 μmol·g⁻¹. According to the capture experiment of active species in the dark, the degradation rates are decreased by 22.75%, 28.43%, 10.44% and 14.66% after adding BQ, Na₂C₂O₄, TBA and CuSO₄, respectively, indicating that the active species degrading antibiotics in the dark are ·O₂, h⁺, OH and e⁻ (Fig. S16).

Based on the above test results, the catalytic mechanism of the BiOBr@Bi₄O₅Br₂ heterojunction in the dark is proposed. Because of the interface electric field formed by the BiOBr@Bi₄O₅Br₂ crystal in the process of forming the diffusion electric double layer, the interface electric field makes the series polarized electric field of the BiOBr@Bi₄O₅Br₂ heterojunction, and the series polarized electric field in heterojunction makes the BiOBr crystal store holes, the Bi₄O₅Br₂ crystal store electrons and the interface store excitons (Fig. 6g). Under the action of mechanical shear force, the strain makes the direction of the series polarized electric field of the heterojunction consistent and further enhances (the red part of the arrow in Fig. 6h), and under the positive piezoelectric effect, the holes stored in the BiOBr crystal quickly are migrated to the surface of the BiOBr (the yellow holes in Fig. 6i), directly degrading pollutants or reacting with H₂O/OH⁻ to generate ·OH radicals. Electrons stored in the Bi₄O₅Br₂ crystal are migrated to the surface of Bi₄O₅Br₂ under the action of the series polarized electric field (the blue electrons in Fig. 6i), react with the dissolved oxygen to form ·O₂ radical, and form ·O₂ with the dissolved oxygen in solution. Part of that electron stored in the BiOBr crystal and part of the hole stored in Bi₄O₅Br₂ rapidly migrate to the interface under the action of the enhanced series polarized electric field, forming excitons (the yellow electrons and the blue colors at the interface in Fig. 6i), resulting in an interfacial polarized electric potential ΔE≠0. If the potential of excitons stored at the interface and the newly formed excitons tends to be ΔE=0, the excitons will migrate to the surface and react with the dissolved oxygen to form ¹O₂ on the surface. In the dark, the formed h⁺, ·O₂, ·OH and ¹O₂ will gradually decompose and mineralize pollutants into H₂O and CO₂.

After many dark cycles, h⁺, e⁻ and h⁺-e⁻ are consumed. After re-illumination, the BiOBr and Bi₄O₅Br₂ in the energy storage BiOBr@Bi₄O₅Br₂ heterojunction are excited by light to generate the photogenerated electrons and holes. Following the Z-scheme heterojunction transfer mechanism, the h⁺ ions are stored in the BiOBr crystal and the e⁻

ions are stored in Bi₄O₅Br₂ under the action of the intrinsic polarized electric field. It recovers its dark degradation ability, releases h⁺, e⁻ and h⁺-e⁻ in the dark, continues the redox reaction, and gradually decomposes and mineralizes pollutants into H₂O and CO₂. Therefore, the prepared energy storage BiOBr@Bi₄O₅Br₂ heterojunction has a recyclable storage mechanism of electrons, holes and excitons.

3.3. Photocatalytic performance

After 25 min of NIR light irradiation, the degradation rates of CIP by BOB, BOB-3, BOB-6, BOB-9, BOB-12 and BOB-14 are 42.39%, 62.80%, 73.29%, 45.32%, 38.63% and 10.06%, respectively (Fig. 7a). The degradation rate constants are 0.02662, 0.04847, 0.06156, 0.02837, 0.02236 and 0.00529 min⁻¹, respectively (Fig. S17a). The TOC removal rates of BOB, BOB-3, BOB-6 and BOB-12 are 14.95%, 43.50%, 50.70% and 13.79%, respectively (the inset in Fig. 7a). After irradiation with monochromatic light of 740 nm, 850 nm, 940 nm and 1100 nm for 50 min, the degradation rates of CIP are 55.28%, 56.24%, 58.46% and 61.99%, respectively (Fig. S17b), which further proves that the BiOBr@Bi₄O₅Br₂ heterojunction has full-spectrum response characteristics and can realize the full-spectrum catalytic pollutant degradation. The degradation rates of CIP by BOB-6 are 73.59%, 69.80%, 64.04%, 62.59% and 62.18%, respectively in five cycles (Fig. 7b). After five cycles, the phase has not changed (Fig. S17c), which shows that BOB has good cycle stability in degrading pollutants under NIR light. The degradation rates of TC, BPA, MB, RhB and MO by BOB-6 are 67.32%, 73.25 min⁻¹, 81.23%, 94.52% and 83.14%, respectively after 25 min of NIR light irradiation (Fig. 7c). Fig. 7d is the absorbance diagram of the UV-vis spectrogram of BOB-6 of the mixed solution of 20 mg·L⁻¹ TC, 10 mg·L⁻¹ CIP, 10 mg·L⁻¹ MB and 10 mg·L⁻¹ RhB. With the extension of degradation time, the absorption band is gradually weakened, and the absorption band basically disappears after 25 min of reaction under NIR light. The TOC removal rate of the mixed solution is 28.78% (the inset in Fig. 7d), which shows that the BiOBr@Bi₄O₅Br₂ heterojunction has the ability to degrade a variety of pollutants under NIR light, and has a broad spectrum, which proves that the energy storage BiOBr@Bi₄O₅Br₂ heterojunction has the full-spectrum and broad-spectrum degradation performance. In order to eliminate the influence of thermal effect caused by LSPR effect on catalysis, when 50 mg of BOB, BOB-6 and BOB-12 are respectively added to 50 mL CIP (10 mg/L) solution, the temperature changes of CIP solution at different degradation reaction times are measured by an infrared thermal imager (an infrared thermography on a FLIR E5 thermal imaging camera) under NIR light irradiation (Fig. S19). Because the heat generated in the reaction is usually thought to be caused by photothermal effect when it is above 20 °C, in this experiment, the photothermal effect does not play a major role in CIP degradation due to the limited temperature rise (< 5.2 °C). Therefore, the thermal effect caused by LSPR effect under near infrared light irradiation can be ignored. A detailed comparison is available in the Supporting Information (Table S1).

The degradation process of CIP by BOB-6 under NIR light is analyzed by LC-MS. (Fig. S20, Fig. S21 and Table S5), BOB-6 degraded CIP into P18(*m/z*=167), P19(*m/z*=114), P20(*m/z*=98), P21(*m/z*=74), P22(*m/z*=60) and so on (Fig. S22) [41]. Finally, it is converted into CO₂ and H₂O. The LC-MS data prove that the BiOBr@Bi₄O₅Br₂ heterojunction has the ability to degrade CIP under NIR light, which further proves that the energy storage BiOBr@Bi₄O₅Br₂ heterojunction has the ability to degrade in full spectrum.

The TEMPO-h⁺ signal appears in BOB-6 after 10 min and 20 min of NIR light irradiation, and the signal is weakened with time, which proves that BOB-6 can generate holes under NIR light (Fig. 8a). BOB-6 can detect the EPR signals corresponding to DMPO-·O₂ and DMPO-·OH after 10 min and 20 min of NIR light irradiation (Fig. 8b-c). It is proved that it can generate ·O₂ and ·OH radicals during the photocatalytic reaction, and the ¹O₂ EPR signal is also detected (Fig. 8d). Due to the Z-scheme charge transfer path is generated in the BOB-6

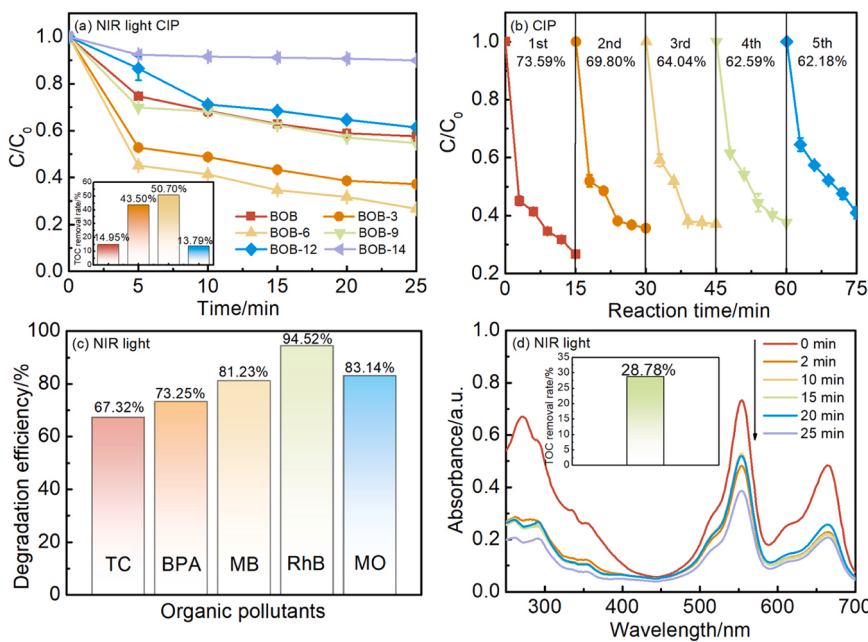


Fig. 7. The effects of the energy storage $\text{BiOBr}@\text{Bi}_4\text{O}_5\text{Br}_2$ heterojunction on CIP under NIR irradiation: (a) degradation activity, (b) degradation cycle experiment, (c) degradation experiment on other pollutants, (d) the absorbance diagram of the UV-vis spectra of the mixed solution.

heterojunction, e^- and h^+ combine at the interface of BOB-6 to produce excitons, and excitons are released to produce $^1\text{O}_2$, which further proves that BOB-6 is a Z-scheme heterojunction. Therefore, under NIR light illumination, BOB-6 can produce various active species such as $\cdot\text{O}_2$, $\cdot\text{OH}$, $^1\text{O}_2$ and h^+ to degrade pollutants. When BQ, $\text{Na}_2\text{C}_2\text{O}_4$ and TBA are added under NIR light irradiation, the contribution degree of active species in the degradation process is $\cdot\text{O}_2 > h^+ > \cdot\text{OH}$ (Fig. S23). Based on the above analysis, the piezoelectric catalytic mechanism of the energy storage $\text{BiOBr}@\text{Bi}_4\text{O}_5\text{Br}_2$ heterojunction under NIR light irradiation is proposed.

Under the action of mechanical shear force, the dynamic strain makes the direction of the series polarized electric field of heterojunction consistent and further enhanced (The red part in the black arrow in Fig. 8f is the enhanced part). Excited by NIR light, all the holes and electrons stored in the BiOBr and $\text{Bi}_4\text{O}_5\text{Br}_2$ crystals in the $\text{BiOBr}@\text{Bi}_4\text{O}_5\text{Br}_2$ heterojunction produce the double LSPR effect, resulting in high-energy hot holes and high-energy hot electrons (the yellow holes with red circles and the blue electrons with red circles in Fig. 8g). Under the action of the series polarized electric field of the heterojunction, high-energy hot holes of BiOBr accelerate to the crystal surface and directly degrade pollutants, while high-energy hot electrons of $\text{Bi}_4\text{O}_5\text{Br}_2$ accelerate to the crystal surface and react with the dissolved oxygen to form high-energy $\cdot\text{O}_2$ free radicals. The series polarized electric field also accelerates the migration of high-energy hot electrons of BiOBr (electrons with red circles in yellow in Fig. 8g) and high-energy hot holes of $\text{Bi}_4\text{O}_5\text{Br}_2$ (holes with red circles in blue in Fig. 8g) to the interface, forming high-energy excitons at the interface. If the potential of high-energy excitons at the interface tends to $\Delta E=0$, the excitons will migrate to react with the dissolved oxygen to form high-energy $^1\text{O}_2$. In Fig. 7a, the fast degradation efficiency of CIP is 54.90% due to the double LSPR effect driven by heterogeneous crystal energy storage piezoelectric catalysis within 1–5 min, which is the effect of energy storage piezoelectric catalysis. With the extension of the irradiation time of NIR light, when the photon vibration frequency of NIR light is the same as that of the defect itself, the surface plasmon resonance will occur. The local magnetic field of h^+ stored in BiOBr (the purple arc in Fig. 8h) acts on $\text{Bi}_4\text{O}_5\text{Br}_2$, and the local magnetic field of e^- stored in $\text{Bi}_4\text{O}_5\text{Br}_2$ (the green arc in Fig. 8h) acts on BiOBr , causing the photo-generated electrons and holes generated by the excitation of BiOBr and

$\text{Bi}_4\text{O}_5\text{Br}_2$ by NIR light. Driven by the heterojunction series polarized electric field, h^+ on the surface of BiOBr and e^- on the surface of $\text{Bi}_4\text{O}_5\text{Br}_2$ crystal, and (h^+e^-) on the interface region are continuously supplemented, and $\cdot\text{O}_2$, h^+ , $\cdot\text{OH}$ and $^1\text{O}_2$ degradation pollutants are continuously formed, which is decomposed and mineralized into H_2O and CO_2 . The energy of h^+ , e^- and (h^+e^-) generated by photogeneration is weak. In Fig. 7a, the degradation rate of the heterogeneous pair CIP is 18.39% in 5–25 min, and the degradation efficiency is gentle, which is the effect of photocatalysis and piezoelectric catalysis. Finally, under the NIR light, the double LSPR effect of heterojunction forms high-energy $\cdot\text{O}_2$, high-energy h^+ , high-energy $\cdot\text{OH}$ and high-energy $^1\text{O}_2$. Driven by photogenerated $\cdot\text{O}_2$, h^+ , $\cdot\text{OH}$ and $^1\text{O}_2$ and heterojunction series polarized electric field, the degradation rate of CIP by heterojunction piezoelectric catalysis can reach 73.29% under the NIR light irradiation for 25 min.

The full-spectrum catalytic performance of the catalyst is evaluated by degrading pollutants, such as CIP under the irradiation of visible light. After 15 min of visible light irradiation, the degradation rates of CIP by BOB, BOB-3, BOB-6, BOB-9, BOB-12 and BOB-14 are 41.36%, 63.70%, 73.59%, 67.10%, 29.80% and 25.17%, respectively (Fig. S24a). The degradation rate constants and the cycle performance are in Supporting Information. (Fig. S24b-c). After 25 min of visible light irradiation, the degradation efficiencies of TC (20 mg·L⁻¹) by BOB, BOB-3, BOB-6, BOB-9, BOB-12 and BOB-14 are 46.12%, 59.49%, 79.40%, 70.34%, 43.76% and 37.54%, respectively (Fig. S24d). The degradation rate constants and the cycle performance are in Supporting Information. (Fig. S24e-f). The comparison of XRD patterns before and after cyclic degradation for five times show that the phase does not change (Fig. S24g), which shows that the $\text{BiOBr}@\text{Bi}_4\text{O}_5\text{Br}_2$ heterojunction has the ability to degrade various pollutants under visible light and has a broad spectrum by adjusting the pH of the precursor solution (Fig. S24h-i). The results of the above photocatalytic experiments show that the formation of the energy storage $\text{BiOBr}@\text{Bi}_4\text{O}_5\text{Br}_2$ heterojunction promotes the separation of carriers, further improving the photocatalytic activity and stabilizing pollutants. The LC-MS spectrum of the CIP degradation solution by BOB-6 under visible light proves that the macromolecular CIP is decomposed rather than adsorbed (Figs. S25–27 and Table S6). The mechanism of the piezoelectric catalytic energy storage of $\text{BiOBr}@\text{Bi}_4\text{O}_5\text{Br}_2$ heterojunction is similar to that of the piezoelectric catalytic energy storage under NIR light except that there is

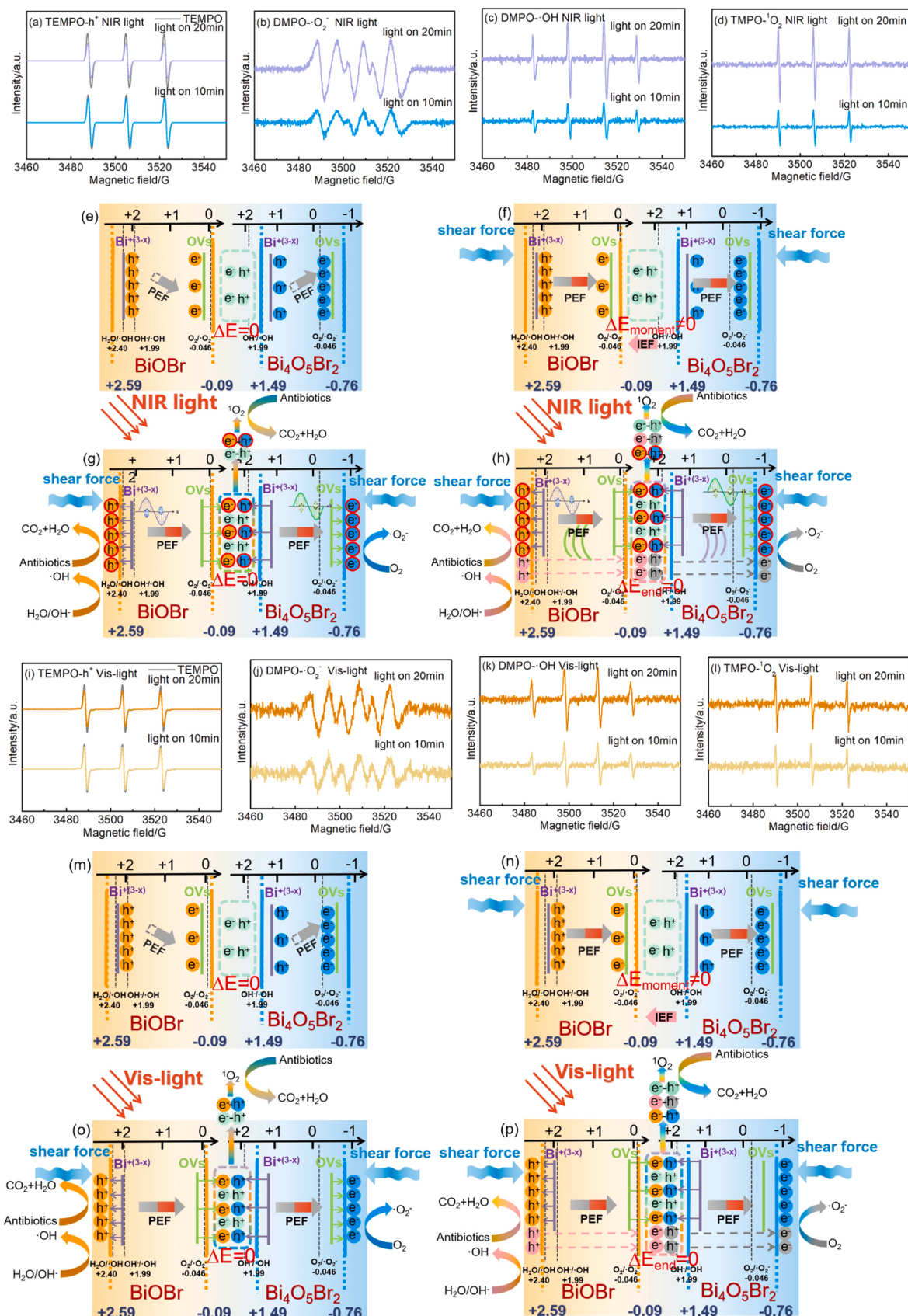


Fig. 8. Energy storage piezoelectric catalytic mechanism of the energy storage $\text{BiOBr}@\text{Bi}_4\text{O}_5\text{Br}_2$ heterojunction under NIR light and visible light: EPR spectrum: (a) and (i) $\text{TEMPO}-\text{h}^+$, (b) and (j) $\text{DMPO}-\text{O}_2^-$, (c) and (k) $\text{DMPO}-\text{OH}$, (d) and (l) $\text{TMPO}-\text{O}_2^-$. (e) and (m) the heterojunction polarization electric field, (f) and (n) the mechanical force enhances polarization electric field, (g) and (o) polarization electric field accelerating high-energy carrier migration, (h) and (p) polarization electric field accelerating photogenerated carrier migration.

no LSPR effect in visible light (Fig. 8i-p, the related discussion is in Supporting Information). The rapid degradation efficiency of CIP by the BiOBr@Bi₄O₅Br₂ heterojunction under visible light irradiation for 15 min and 1–3 min is the effect of the energy storage piezoelectric catalysis, and the degradation rate is 52.1%. During 3–15 min, the gentle degradation efficiency of CIP is due to the effects of photocatalysis and piezoelectric catalysis, and the degradation rate is 21.49% (Fig. S24a).

The separation, transfer and recombination behavior of the photo-generated carriers in the samples are characterized by photoelectrochemical tests. Fig. S29a and Fig. S29b are transient photocurrent response curves of samples irradiated by visible light and NIR light, and all the samples show the rapid, stable and repeatable photocurrent response. BOB-6 shows the highest optical flow density under the irradiation of visible light and NIR light. The BiOBr@Bi₄O₅Br₂ heterostructure can promote the separation and migration of the photogenerated carriers and inhibit the recombination of carriers. All the samples show the rapid, stable and repeatable photocurrent response, and the optical flow curve immediately reappears and remains stable at the moment of turning on the light, indicating that the prepared samples have good photophysical stability. The EIS diagram is fitted by ZsimpWin software (Table S7), and BOB-6 has the smallest charge transfer resistance value, corresponding to its maximum transient photocurrent value (Fig. S29c). The optical properties of the sample are further characterized by PL spectrum (Fig. S30a). The sample has a strong fluorescence emission peak in the range of 510–530 nm. The obvious PL quenching of BOB-3 and BOB-6 indicates that the formation of heterojunction can significantly improve the separation efficiency of the photogenerated electron-hole pairs of BiOBr and Bi₄O₅Br₂. The relaxation kinetics of the photogenerated carriers is further characterized by TR-PL spectrum (Fig. S30b). The lifetimes of the photogenerated carriers of BOB-3 and BOB-6 are significantly longer than those of BOB and BOB-12, which further indicates that the separation efficiencies of the photogenerated electron-hole pairs in the BiOBr@Bi₄O₅Br₂ heterojunction are significantly higher than those of single-component BiOBr and Bi₄O₅Br₂.

4. Conclusion

The energy storage BiOBr@Bi₄O₅Br₂ heterojunction piezoelectric catalyst for storing electrons, holes and excitons is prepared by homogeneous nucleation and crystallization in hydrothermal system by adjusting the pH of the precursor solution. The Z-scheme interface electric field of heterojunction enhances the polarization electric field and the piezoelectric effect of heterojunction. The concentrations of the stored electrons and holes are 94.23 $\mu\text{mol g}^{-1}$ and 86.17 $\mu\text{mol g}^{-1}$, respectively, and d_{33} is increased to 6.29 nm V^{-1} , and the concentrations of the stored electrons (holes) are 2.03 times (1.34 times) and 2.33 times (1.34 times) those of BiOBr and Bi₄O₅Br₂, respectively. The energy storage and positive piezoelectric effect makes the heterojunction degrade antibiotics and organic pollutants, such as TC, CIP, BPA, MB, RhB and MO by 63.44%, 75.95%, 73.90%, 81.06%, 94.70% and 75.81%, respectively in the dark, and the energy storage BiOBr@Bi₄O₅Br₂ heterojunction has good dark cycle stability and dark repair. The double LSPR effect of storing electrons and holes and the series polarized electric field enhanced by heterojunction strain accelerate the migration rate of the stored electrons, holes and excitons. The positive piezoelectric effect and energy storage make the heterojunction degrade TC, CIP, BPA, MB, RhB and MO by 79.40%/67.32%, 73.59%/73.29%, 74.05%/73.25%, 82.78%/81.23%, 94.43%/94.52% and 87.24%/83.14%, respectively under visible light/NIR light. This work provides a new idea for the preparation of all-weather energy storage piezoelectric catalytic materials by using the traditional bismuth-based nanomaterials with the intrinsic polarization electric field as energy storage heterojunction.

CRediT authorship contribution statement

Zeqiong Wang: Project administration, Software. **Xiongtao Wu:** Software, Validation. **Linxin Guo:** Software, Visualization. **Chunyan Zeng:** Investigation, Visualization. **Ying Liu:** Formal analysis. **Tian Liu:** Investigation. **Qian Yang:** Methodology, Visualization. **Lixiong Yin:** Resources. **Wenlong Liu:** Funding acquisition, Supervision. **Bixin Zhang:** Writing – original draft, Data curation, Conceptualization. **Huijun Ren:** Supervision, Writing – review & editing. **Guoqiang Tan:** Writing – review & editing, Funding acquisition. **Sizhe Fan:** Investigation, Software. **Ao Xia:** Supervision, Funding acquisition.

Declaration of Competing Interest

The authors declare that they have no known competing financial interests or personal relationships that could have appeared to influence the work reported in this paper.

Data Availability

Data will be made available on request.

Acknowledgements

This work was financially supported by the National Natural Science Foundation of China (Grant No. 52172215 and 52372207), Shaanxi Province Key R&D Program (2022GY-428), the Youth Innovation Team of Shaanxi Universities (2022-70) and the Graduate Innovation Fund of Shaanxi University of Science and Technology (SUST-A04).

Appendix A. Supporting information

Supplementary data associated with this article can be found in the online version at [doi:10.1016/j.apcatb.2024.124021](https://doi.org/10.1016/j.apcatb.2024.124021).

References

- [1] W. Zhang, Y. Peng, Y. Yang, L. Zhang, Z. Bian, H. Wang, Bismuth-rich strategy intensifies the molecular oxygen activation and internal electrical field for the photocatalytic degradation of tetracycline hydrochloride, *Chem. Eng. J.* 430 (2022).
- [2] D. Jiang, T. Wang, Q. Xu, D. Li, S. Meng, M. Chen, Perovskite oxide ultrathin nanosheets/g-C₃N₄ 2D-2D heterojunction photocatalysts with significantly enhanced photocatalytic activity towards the photodegradation of tetracycline, *Appl. Catal. B Environ.* 201 (2017) 617–628.
- [3] Ad.O. Jorgetto, M.V. Boldrin Zanoni, M.O. Orlandi, Assessment of the superior photocatalytic properties of Sn²⁺-containing SnO₂ microrods on the photodegradation of methyl orange, *Sci. Rep.* 13 (2023).
- [4] Y. Jin, F. Li, T. Li, X. Xing, W. Fan, L. Zhang, C. Hu, Enhanced internal electric field in S-doped BiOBr for intercalation, adsorption and degradation of ciprofloxacin by photoinitiation, *Appl. Catal. B Environ.* 302 (2022).
- [5] Z. Luo, X. Ye, S. Zhang, S. Xue, C. Yang, Y. Hou, W. Xing, R. Yu, J. Sun, Z. Yu, X. Wang, Unveiling the charge transfer dynamics steered by built-in electric fields in BiOBr photocatalysts, *Nat. Commun.* 13 (2022) 2230.
- [6] H. Cheng, B. Huang, Y. Dai, Engineering BiOX (X = Cl, Br, I) nanostructures for highly efficient photocatalytic applications, *Nanoscale* 6 (2014) 2009–2026.
- [7] D. Mao, S. Ding, L. Meng, Y. Dai, C. Sun, S. Yang, H. He, One-pot microemulsion-mediated synthesis of Bi-rich Bi₄O₅Br₂ with controllable morphologies and excellent visible-light photocatalytic removal of pollutants, *Appl. Catal. B Environ.* 207 (2017) 153–165.
- [8] Y. Guo, W. Shi, Y. Zhu, Y. Xu, F. Cui, Enhanced photoactivity and oxidizing ability simultaneously via internal electric field and valence band position by crystal structure of bismuth oxyiodide, *Appl. Catal. B Environ.* 262 (2020).
- [9] J. Di, J. Xia, M.F. Chisholm, J. Zhong, C. Chen, X. Cao, F. Dong, Z. Chi, H. Chen, Y. X. Weng, J. Xiong, S.Z. Yang, H. Li, Z. Liu, S. Dai, Defect-tailoring mediated electron-hole separation in single-unit-cell Bi₃O₄Br nanosheets for boosting photocatalytic hydrogen evolution and nitrogen fixation, *Adv. Mater.* 31 (2019).
- [10] B. Wang, J. Zhao, H. Chen, Y.-X. Weng, H. Tang, Z. Chen, W. Zhu, Y. She, J. Xia, H. Li, Unique Z-scheme carbonized polymer dots/Bi₄O₅Br₂ hybrids for efficiently boosting photocatalytic CO₂ reduction, *Appl. Catal. B Environ.* 293 (2021).
- [11] Y. Wang, K. Wang, J. Meng, C. Ban, Y. Duan, Y. Feng, S. Jing, J. Ma, D. Yu, L. Gan, X. Zhou, Constructing atomic surface concaves on Bi₅O₇Br nanotube for efficient photocatalytic CO₂ reduction, *Nano Energy* 109 (2023).

[12] Q. Han, K. Zhang, J. Zhang, S. Gong, X. Wang, J. Zhu, Effect of the counter ions on composition and morphology of bismuth oxyhalides and their photocatalytic performance, *Chem. Eng. J.* 299 (2016) 217–226.

[13] J. Shang, W. Hao, X. Lv, T. Wang, X. Wang, Y. Du, S. Dou, T. Xie, D. Wang, J. Wang, Bismuth oxybromide with reasonable photocatalytic reduction activity under visible light, *ACS. Catal.* 4 (2014) 954–961.

[14] J. Xiong, P. Song, J. Di, H. Li, Bismuth-rich bismuth oxyhalides: a new opportunity to trigger high-efficiency photocatalysis, *J. Mater. Chem. A* 8 (2020) 21434–21454.

[15] Z. Wu, J. Shen, N. Ma, Z. Li, M. Wu, D. Xu, S. Zhang, W. Feng, Y. Zhu, $\text{Bi}_4\text{O}_5\text{Br}_2$ nanosheets with vertical aligned facets for efficient visible-light-driven photodegradation of BPA, *Appl. Catal. B Environ.* 286 (2021).

[16] L. Zhang, X. Yue, J. Liu, J. Feng, X. Zhang, C. Zhang, R. Li, C. Fan, Facile synthesis of $\text{Bi}_5\text{O}_7\text{Br}/\text{BiOBr}$ 2D/3D heterojunction as efficient visible-light-driven photocatalyst for pharmaceutical organic degradation, *Sep. Purif. Technol.* 231 (2020).

[17] Y. Peng, P.-P. Yu, Q.-G. Chen, H.-Y. Zhou, A.-W. Xu, Facile fabrication of $\text{Bi}_{12}\text{O}_7\text{Br}_2/\text{Bi}_{24}\text{O}_{31}\text{Br}_{10}$ Type II heterostructures with high visible photocatalytic activity, *J. Phys. Chem. C.* 119 (2015) 13032–13040.

[18] R. Li, F. Xie, J. Liu, C. Zhang, X. Zhang, C. Fan, Room-temperature hydrolysis fabrication of $\text{BiOBr}/\text{Bi}_{12}\text{O}_7\text{Br}_2$ Z-Scheme photocatalyst with enhanced resorcinol degradation and NO removal activity, *Chemosphere* 235 (2019) 767–775.

[19] T. Liu, G. Tan, S. Feng, B. Zhang, Y. Liu, Z. Wang, Y. Bi, Q. Yang, A. Xia, W. Liu, H. Ren, L. Lv, Dual Localized Surface Plasmon Resonance effect enhances $\text{Nb}_2\text{AlC}/\text{Nb}_2\text{C}$ MXene thermally coupled photocatalytic reduction of CO_2 hydrogenation activity, *J. Colloid Inter. Sci.* 652 (2023) 599–611.

[20] Emiko Kazuma, Jae-hoon Jung, Hiromu Ueba, Michael Trenary, Y. Kim, Real-space and real-time observation of a plasmon-induced chemical reaction of a single molecule, *Science* 360 (2018) 521–526.

[21] B. Zhang, Y. Wang, Z. Wang, G. Tan, T. Liu, S. Feng, Y. Tan, W. Liu, Q. Yang, Y. Liu, A. Xia, H. Ren, Y. Wu, Surface plasmon resonance effects of Ti_3C_2 MXene for degradation of antibiotics under full spectrum, *Appl. Catal. B Environ.* 339 (2023).

[22] Y. Lu, X. Jia, Z. Ma, Y. Li, S. Yue, X. Liu, J. Zhang, $\text{W}^{5+} - \text{W}^{5+}$ pair induced LSPR of $\text{W}_{18}\text{O}_{49}$ to sensitize ZnIn_2S_4 for full-spectrum solar-light-driven photocatalytic hydrogen evolution, *Adv. Funct. Mater.* 32 (2022).

[23] J. Li, W. Pan, Q. Liu, Z. Chen, Z. Chen, X. Feng, H. Chen, Interfacial engineering of $\text{Bi}_{19}\text{Br}_9\text{S}_{27}$ nanowires promotes metallic photocatalytic CO_2 reduction activity under near-infrared light irradiation, *J. Am. Chem. Soc.* 143 (2021) 6551–6559.

[24] M. Wang, G. Tan, B. Zhang, Y. Wang, Y. Bi, Q. Yang, Y. Liu, T. Liu, Z. Wang, H. Ren, L. Lv, A. Xia, L. Yin, Q. Yuan, W. Liu, Y. Liu, Synergistic integration of energy storage catalysis: a multifunctional catalytic material for round-the-clock environmental cleaning, *Appl. Catal. B Environ.* 321 (2023).

[25] J. Yan, C. Wang, H. Ma, Y. Li, Y. Liu, N. Suzuki, C. Terashima, A. Fujishima, X. Zhang, Photothermal synergic enhancement of direct Z-scheme behavior of $\text{Bi}_4\text{Ta}_8\text{Cl}/\text{W}_{18}\text{O}_{49}$ heterostructure for CO_2 reduction, *Appl. Catal. B Environ.* 268 (2020).

[26] Y. Li, L. Chen, Y. Guo, X. Sun, Y. Wei, Preparation and characterization of WO_3/TiO_2 hollow microsphere composites with catalytic activity in dark, *Chem. Eng. J.* 181–182 (2012) 734–739.

[27] Z. Wang, G. Tan, B. Zhang, Q. Yang, S. Feng, Y. Liu, T. Liu, L. Guo, C. Zeng, W. Liu, A. Xia, H. Ren, L. Yin, S. Fan, Intrinsic polarised electric field induces a storing mechanism to achieve energy storing catalysis in V_2C MXene, *Adv. Mater.* (2023).

[28] M. Wang, G. Tan, H. Ren, L. Lv, A. Xia, Enhancement mechanism of full-solar-spectrum catalytic activity of $\text{g-C}_3\text{N}_{4-x}/\text{Bi}/\text{Bi}_2\text{O}_2(\text{CO}_3)_{1-x}(\text{Br}, \text{I})_x$ heterojunction: the roles of plasma Bi and oxygen vacancies, *Chem. Eng. J.* 430 (2022).

[29] J. Sun, X. Li, Q. Zhao, B. Liu, Ultrathin nanoflake-assembled hierarchical BiOBr microflower with highly exposed {001} facets for efficient photocatalytic degradation of gaseous ortho-dichlorobenzene, *Appl. Catal. B Environ.* 281 (2021).

[30] J. Jing, J. Yang, Z. Zhang, Y. Zhu, Supramolecular zinc porphyrin photocatalyst with strong reduction ability and robust built-in electric field for highly efficient hydrogen production, *Adv. Energy Mater.* 11 (2021).

[31] Q. Yang, G. Tan, L. Yin, W. Liu, B. Zhang, S. Feng, Y. Bi, Y. Liu, T. Liu, Z. Wang, H. Ren, A. Xia, Full-spectrum broad-spectrum degradation of antibiotics by $\text{BiVO}_4@\text{BiOCl}$ crystal plane S-type and Z-type heterojunctions, *Chem. Eng. J.* 467 (2023).

[32] H. You, Z. Wu, L. Zhang, Y. Ying, Y. Liu, L. Fei, X. Chen, Y. Jia, Y. Wang, F. Wang, S. Ju, J. Qiao, C.H. Lam, H. Huang, Harvesting the vibration energy of BiFeO_3 nanosheets for hydrogen evolution, *Angew. Chem. Int. Ed.* 58 (2019) 11779–11784.

[33] J. He, Y. Liu, J. Qu, H. Xie, R. Lu, F. Fan, C. Li, Boosting photocatalytic water oxidation on photocatalysts with ferroelectric single domains, *Adv. Mater.* 35 (2023) 2210374.

[34] L. Yang, B. Tian, Y. Xie, S. Dong, M. Yang, S. Gai, J. Lin, Oxygen-vacancy-rich piezoelectric BiO_{2-x} nanosheets for augmented piezocatalytic, sonochemical, and enzymatic therapies, *Adv. Mater.* 35 (2023) 2300648.

[35] J. Yuan, W. Feng, Y. Zhang, J. Xiao, X. Zhang, Y. Wu, W. Ni, H. Huang, W. Dai, Unraveling synergistic effect of defects and piezoelectric field in breakthrough piezo-photocatalytic N_2 reduction, *Adv. Mater.* (2023).

[36] Y. Liu, G. Tan, S. Feng, B. Zhang, T. Liu, Z. Wang, Y. Bi, Q. Yang, H. Ren, L. Lv, W. Liu, A. Xia, Q. Zhao, Localized surface plasmon resonance effect of V_4C_3 -MXene for enhancing photothermal reduction of CO_2 in full solar spectrum, *Sep. Purif. Technol.* 326 (2023).

[37] C. Porwal, S. Verma, M. Kumar, A. Gaur, V.S. Chauhan, R. Vaish, I. Kabaili, I. Boukhris, H.K.B. Park, Y.H. Joo, T.H. Sung, A. Kumar, Electrospun membrane of bismuth vanadate-polyvinylidene fluoride nanofibers for efficient piezo-photocatalysis applications, *Sci. Rep.* 13 (2023).

[38] T. An, H. Yang, G. Li, W. Song, W.J. Cooper, X. Nie, Kinetics and mechanism of advanced oxidation processes (AOPs) in degradation of ciprofloxacin in water, *Appl. Catal. B Environ.* 94 (2010) 288–294.

[39] Q. Yan, Y. Fu, Y. Zhang, H. Wang, S. Wang, W. Cui, $\text{Ag}/\gamma\text{-AgI}/\text{Bi}_2\text{O}_3\text{CO}_3/\text{Bi}$ S-scheme heterojunction with enhanced photocatalyst performance, *Sep. Purif. Technol.* 263 (2021).

[40] Q. Yang, G. Tan, L. Yin, W. Liu, B. Zhang, S. Feng, Y. Bi, Y. Liu, T. Liu, Z. Wang, H. Ren, A. Xia, Full-spectrum broad-spectrum degradation of antibiotics by $\text{BiVO}_4@\text{BiOCl}$ crystal plane S-type and Z-type heterojunctions, *Chem. Eng. J.* 467 (2023).

[41] A.S. Giri, A.K. Golder, Ciprofloxacin degradation from aqueous solution by Fenton oxidation: reaction kinetics and degradation mechanisms, *RSC Adv.* 4 (2014).